



In vivo corneal and lenticular microscopy with asymmetric fundus retroillumination

TIMOTHY D. WEBER^{1,*}  AND JEROME MERTZ^{1,2} 

¹Department of Biomedical Engineering, Boston University, 44 Cummington Mall, Boston, MA 02215, USA

²Photonics Center, Boston University, 8 Saint Mary's Street, Boston, MA 02215, USA

*tweber@bu.edu

Abstract: We describe a new technique for non-contact *in vivo* corneal and lenticular microscopy. It is based on fundus retro-reflection and back-illumination of the crystalline lens and cornea. To enhance phase-gradient contrast, we apply asymmetric illumination by illuminating one side of the fundus. The technique produces micron-scale lateral resolution images across a 1 mm diagonal field of view in the central cornea. We show representative images of the epithelium, the subbasal nerve plexus, large stromal nerves, dendritic immune cells, endothelial nuclei, and the anterior crystalline lens, demonstrating the potential of this instrument for clinical applications.

© 2020 Optical Society of America under the terms of the [OSA Open Access Publishing Agreement](#)

1. Introduction

Non-invasive cellular-scale imaging of the cornea is a valuable tool for disease diagnostics, management, and monitoring. In clinical practice, it is often used to distinguish forms of microbial keratitis *in situ*, when corneal biopsy is either infeasible or fails to yield a diagnosis [1]. It is used routinely to examine the endothelium for evidence of structural change or dysfunction, which can cause corneal edema and concomitant vision impairment [2]. Cellular-scale corneal nerve imaging has also been suggested as a means to monitor systemic disease, such as diabetes mellitus, or recovery from refractive surgery [3].

Currently, the established microscopic clinical imaging methods are specular microscopy (SM) [4] and *in vivo* confocal microscopy (IVCM) [5]. Whereas SM is restricted to the endothelium, IVCM is able to produce high contrast images throughout the full thickness of the human cornea and resolve nerves and cells in 3D [6]. A caveat is that IVCM is usually performed in contact with the cornea, meaning the objective lens (or protective cap) touches the cornea during the examination. Topical anesthetic must be administered prior to imaging. With an experienced technician, contact operation is safe and straightforward. Nevertheless, there are many subjects with phobias that will not tolerate contact operation. Moreover, for routine screening purposes where speed is critical, non-contact methods are highly desired.

Much of the recent progress in non-contact *in vivo* corneal imaging has involved various flavors of optical coherent tomography (OCT) [7,8], largely due to its remarkable depth selectivity. Chen et al. described a micro-OCT system capable of cross-sectional swine cornea imaging [9]. However, the A-line rate was not fast enough to provide useful *en face* images in the presence of motion. Mazlin and colleagues took a different approach and applied a parallelized full-field version of time-domain OCT (TD-FF-OCT). They were able to acquire very large *en face* images in human cornea [10]. With faster A-line rates, Tan et al. later showed high-resolution imaging in 3D was feasible with point-scanned spectral-domain OCT [11]. With careful motion compensation, Yao et al. examined the monkey corneal endothelium with ultrahigh resolution OCT [12]. Gabor-domain optical coherence microscopy has also been successfully demonstrated *in vivo*, albeit only in anesthetized mice [13]. Recently, Auksoy et al. introduced modifications to Fourier-domain full-field OCT (FD-FF-OCT) which enabled volumetric corneal imaging [14].

All the techniques mentioned so far are based on reflection, or, more precisely, backscattered light from corneal microstructures. Here we introduce an *in vivo* microscopy technique based

instead on transmitted light. We call this approach retroillumination microscopy, in deference to the related but lower-resolution slit lamp technique [15]. The key idea is to use the ocular fundus as a diffuse back-reflector, thereby folding the light path of a widefield transmission microscope into one which requires access to only one side of the sample (either the cornea or crystalline lens). To maximize back-reflection, we use near-infrared (NIR) light, which is weakly absorbed in the fundus and virtually undetectable to the subject. Additionally, we implement asymmetric illumination, a well-established method for enhancing intrinsic phase-gradient contrast [16–18]. Our method is non-contact and produces images with high lateral resolution, comparable to state-of-the-art IVCN systems, and across a large field in the central cornea (1 mm diagonal). A strength of the system is its instrumental simplicity, making it a promising candidate for disease screening or global-health applications.

The purpose of this report is to describe the retroillumination microscope design in detail. We also present representative images of the cornea and lens obtained from healthy volunteer subjects.

2. Device description

2.1. Hardware

A schematic for the retroillumination microscope is given in Fig. 1 and cross-sectional illustrations of the illumination beam at the cornea and fundus are given in Fig. 2. The subject is seated in a darkened room in front of the microscope. The subject's head is placed on a chin rest, while their gaze is stabilized with a dim external fixation target. The microscope is mounted on translation stages for alignment with the eye.

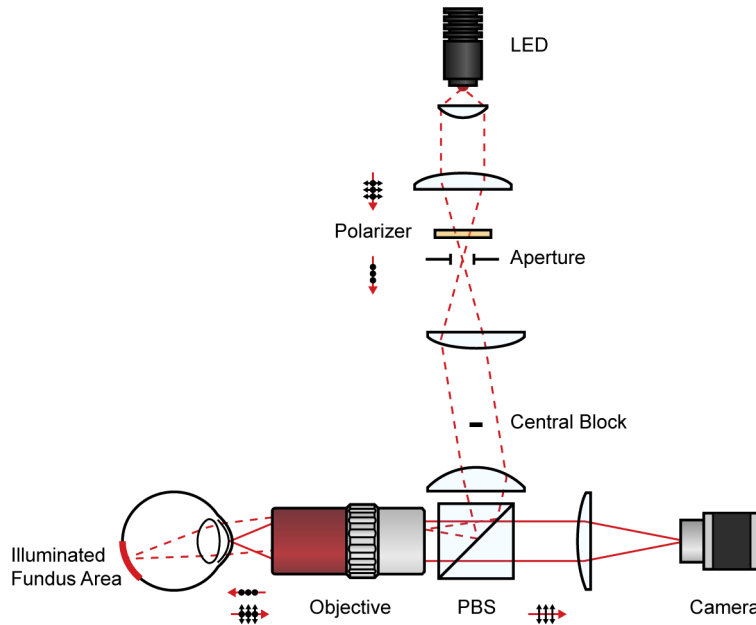


Fig. 1. System optical diagram. PBS: Polarizing beamsplitter.

Illumination consists of a high power NIR LED (LZ1-10R602, Osram; 850 nm center wavelength), which is offset and magnified to span a semi-circular aperture and subsequently relayed through a beamsplitter to the back focal plane of a long working distance objective lens (MPlanApoNIR 20X/0.4, Mitutoyo). The diameter of the aperture is adjusted such that its image

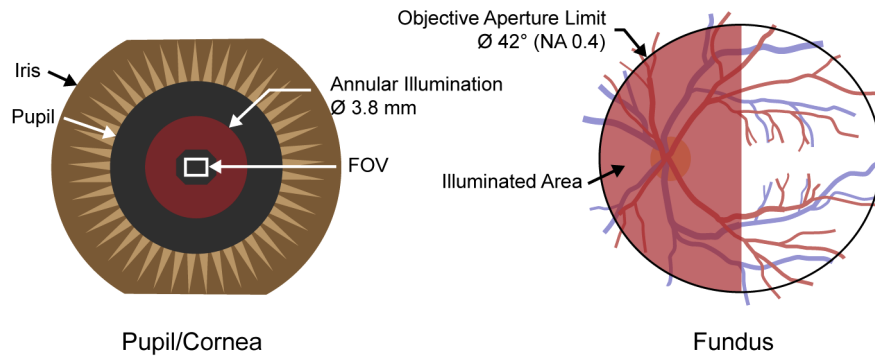


Fig. 2. Illumination beam, shown in red, at the pupil/cornea (left) and at the fundus (right). Diffusely reflected light from the fundus retroilluminates the central cornea including the microscope field of view (FOV).

half fills the objective's back aperture. The objective lens then projects the semi-circular LED image onto the fundus with a visual angle of about 42° (right side of Fig. 2). The beam diameter at the pupil is about 3.8 mm (Fig. 2, left). The objective lens working distance is 20 mm, which allows the subject to freely blink.

We assume the fundus acts as a spatially uniform diffuse reflector. Features such as retinal vessels and the optic nerve head exhibit rather weak contrast with NIR illumination [19] and hence can be ignored. Reflected light from the fundus obliquely transilluminates (i.e. retroilluminates) the anterior segment. Rays clearing the iris are collected by the same objective and magnified onto the sensor of a machine vision camera (acA2000-340kmNIR, Basler), running at 348 frames/sec. We chose this speed based on speeds used successfully in corneal TD-FF-OCT [10]. We used two off-the-shelf achromats (AC508-300-B and AC508-150-B, Thorlabs) spaced by about 2 mm to achieve the desired tube lens power while avoiding additional aberration.

The system described thus far is susceptible to direct backreflections from the objective and to a lesser extent, the anterior segment interfaces, which can severely impair image contrast. To mitigate direct backreflections, we use cross-polarized detection and exploit the fact that multiple scattering in the fundus largely depolarizes the retro-scattered illumination. Specifically, the LED light is linearly polarized (LPVIS100-MP2, Thorlabs) and combined with a polarizing beamsplitter cube (PBS252, Thorlabs).

In the illumination path, we also insert a small central block (mounted on a transparent window) conjugate to the cornea in order to darken the microscopy field of view (FOV) and reduce depolarized stray light. The block is responsible for the octagon-shaped hole in the incident illumination on the left in Fig. 2. Although this configuration resembles an ophthalmoscope configuration, with its spatially segmented input and output beams, we emphasize that the retroillumination microscope is focused on the anterior segment FOV, not the fundus.

In practice, it is difficult to align the microscope to the eye using only the high-resolution FOV. We obtain a wider field for alignment by using an auxiliary camera to image the subject's pupil with ambient light. Specifically, a motorized flip mirror is inserted in the illumination path just after the aperture (omitted from Fig. 1 for clarity), which temporarily redirects an approximately 7 mm diameter low-resolution image of the pupil onto a free-running machine vision camera (DCC3240N equipped with camera lens MVL6WA, Thorlabs). We use the edges of the subject's iris to then center the microscope prior to microscopic imaging. After locating the desired structures, we usually capture sets of 1024 frames (3 sec video).

2.2. Resolution and field of view

In the asymmetric retroillumination microscope, and indeed all microscopes based on asymmetric illumination, the phase-to-intensity point spread function is no longer an Airy pattern, making it difficult to ascribe a resolution based on, for instance, the Rayleigh criterion. Instead we report spatial frequency bandwidth as a surrogate for resolution. For 850 nm light and 0.4 NA (both illumination and detection), the maximum spatial frequency is laterally 940 mm^{-1} (1.1 μm period) and axially 98 mm^{-1} (10 μm period), in air. For a prescription on how to derive the 3D phase optical transfer function (OTF), see Ref. [20]. Note that the axial discrimination of our microscope is somewhat better than other widefield techniques (e.g. absorption or fluorescence) because the value of the phase OTF is zero at the origin. As a result the OTF acts like a high-pass filter and only reveals high spatial frequencies. High frequencies are only apparent when in focus.

The camera produced images of dimensions 1540 x 1088 pixels. This corresponds to a field of view (FOV) of about 820 x 580 μm (or 1 mm diagonal) in the cornea.

2.3. Light levels and safety

The total incident light power on the cornea is about 50-100 mW, or in terms of irradiance, 0.5-1 W/cm^2 . This light level (at 850 nm) does not cause significant pupil contraction and is just barely visible to the subject. Because the power is distributed over area (see Fig. 2), the corneal and retinal irradiances are below the limits for non-hazardous Group 1 devices in the latest ophthalmic safety standard, the ANSI Z80.36-2016.

3. Image processing

Even with asymmetric retroillumination, intensity contrast at the image plane is low ($<5\%$). Two major sources of noise restrict useful post-hoc expansion of this range: photo response non-uniformity (PRNU) and shot noise. Note that offset noise is corrected on chip with correlated double sampling. Read and quantization noise are negligible. PRNU results from varying pixel gain and is easily corrected by dividing each raw frame by a calibration frame. We use a 256 frame average of uniform intensity, near the expected signal level, as the calibration frame.

Averaging several frames (equivalent to integrating more photons) reduces shot noise, but increases susceptibility to motion blur. Nevertheless, we could still average several frames by registering frames prior to averaging. Registration is performed with standard FFT-based phase-correlation methods [21]. We found that we can usually average at least 9 frames before axial motion decorrelates the FOV.

Additionally, we remove any slowly-varying illumination gradients by dividing the image by a Gaussian-filtered version of itself ($\sigma = 24$ pixels or 13 μm in the cornea). Processing is performed efficiently in a consumer GPU and a cropped version of the images is displayed in real time at approximately 20 Hz. Following acquisition, we perform the same processing on the full FOV and for each frame in the stack.

To quantify nerve density, we used the NeuronJ plugin [22] to ImageJ [23] to semi-automatically guide nerve tracing and report total nerve length in the FOV. Depending on the chosen neurite contrast setting, the program traced along either the bright or dark edge of the nerve. To assess endothelial cell density, we manually counted cell nuclei by scrolling through a video which had been laterally stabilized with the StackReg plugin [24].

4. Example images

4.1. Subjects

We imaged the left eye of 3 healthy volunteers ranging in age from 26 to 57 and with varying fundus pigmentation. For each subject, informed consent was obtained prior to imaging. The

research was approved by the Boston University Institutional Review Board and conformed to the principles stated in the Declaration of Helsinki.

4.2. Epithelium

The subbasal nerve plexus (SBP) was the most visible structure observed in the epithelium. The SBP is a highly-branched network of nerve fibers located in a narrow plane between the basal epithelial cell layer and Bowman's layer. Figure 3(A) shows the SBP across nearly the entire FOV in the central cornea of a 28-year-old male. The calculated nerve density in this field is 18 mm/mm^2 . This is within the normal range of densities reporting using IVCN (mean: 19 mm/mm^2 , SD: $4\text{--}5 \text{ mm/mm}^2$ [25]).

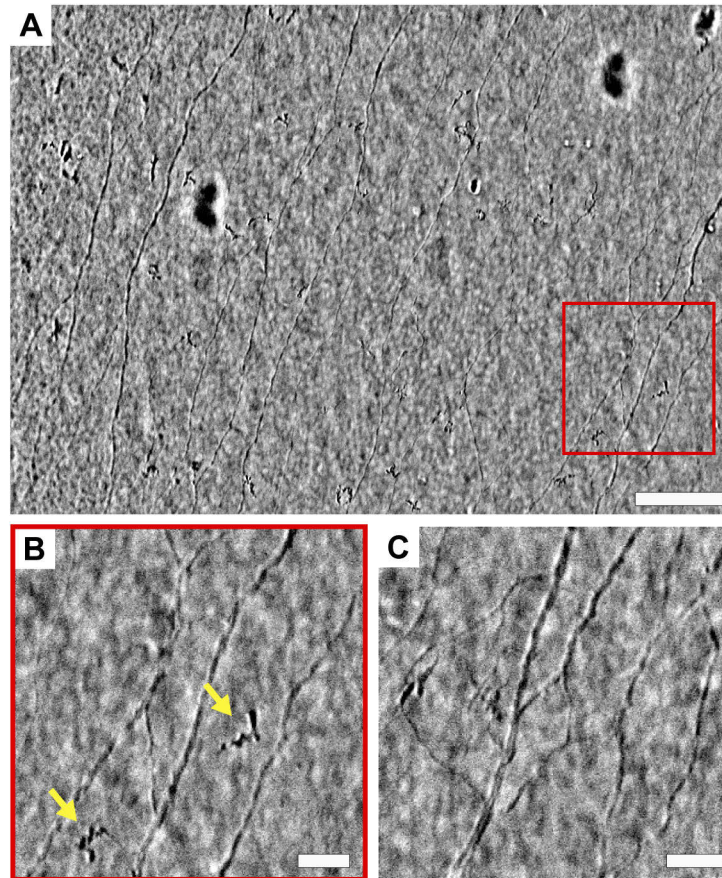


Fig. 3. Subbasal nerve plexus of a 28-year-old male in the central cornea. (A) Full FOV ($820 \times 580 \mu\text{m}$) and (B) indicated area in detail. Arrows indicate suspected dendritic cells. See [Visualization 1](#) for a laterally-stabilized video excerpt. (C) A separate area seen later in the image sequence showing complex anastomoses. Scale bars: (A) $100 \mu\text{m}$, (B) & (C) $25 \mu\text{m}$.

The large dark spots are out-of-focus aggregates of either mucin or shedded epithelial cell debris on the superficial cornea, anterior to the focal plane. These spots appear dark because the aggregates scatter light outside the collection aperture resulting in a decrease in local image intensity. The aggregates usually shift over time and move rapidly following a blink.

Enlarged areas are given in Fig. 3(B) & (C) showing the complex SBP branching and variation of fiber diameter. We also repeatedly saw jagged structures (yellow arrows) near or just anterior to the SBP plane of focus. These structures are more discernible in the video. We believe they are immature dendritic cells [26] which have migrated into the central cornea.

Other periepithelial features are shown in Fig. 4. The tear layer has a punctate appearance (Fig. 4(A)) with sparse highly-scattering aggregates. The edges of squamous and wing epithelial cells are occasionally visible (Fig. 4(B)), but have low contrast and are therefore difficult to distinguish. The basal epithelial cell mosaic (Fig. 4(C)) is always visible with positive or negative contrast depending on the relative position in the focal plane. In one subject, we saw numerous dendritic cells with clearly resolvable cell bodies and large dendrites (Fig. 4(D)). The morphology of these cells is consistent with the mature dendritic cell phenotype, which are more prevalent in the inflamed cornea [26]. We were unable to detect any discernible features in Bowman's layer.

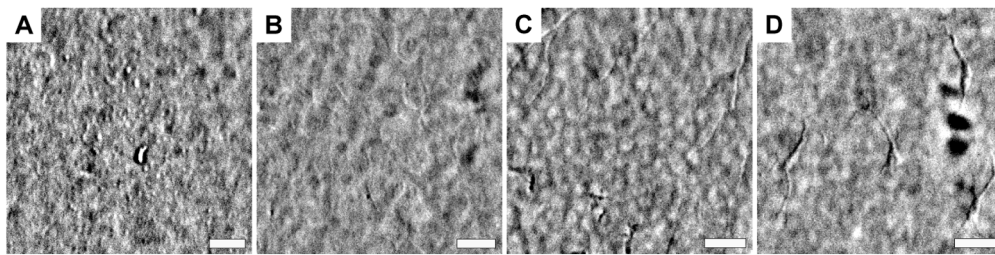


Fig. 4. Other epithelial structures. (A) The tear layer of a 26-year-old female. (B) Superficial and (C) basal epithelial cells in a 28-year-old male. (D) Dendritic immune cells in a 57-year-old male. Scale bars: 25 μ m.

4.3. Stroma

Within the stroma, we observed large branching nerves. In contrast to subbasal nerves, which are largely confined to a single layer, stromal nerves are distributed volumetrically throughout the anterior two-thirds of the stroma [27]. Hence, it was challenging to obtain images where large portions of the nerve were in focus. Figure 5 shows a few stromal nerve segments. Panels A and B are cropped views of the same stromal nerve trunk but at slightly different focal planes. Arrows indicate the common branch point.

Keratocyte nuclei were notably absent from our retroillumination images. This was surprising based on their density in the stroma and high contrast in IVCN [5]. In video sequences, we occasionally observed distinct structures about the size of a cell, but in much lower abundance than expected for normal keratocytes. We also did not see any indication of the subepithelial nerve plexus, however we confined our imaging to the central cornea where the subepithelial plexus may simply be absent [27].

4.4. Endothelium

The endothelium, a monolayer of cells that coats the posterior surface of the cornea, was readily visible with retroillumination. A widefield 1 mm diameter view is shown in Fig. 6. Interestingly, it appears that endothelial cell nuclei, and not cell edges, exhibit the best contrast. Similar to basal epithelial cells, when endothelial cell nuclei are above (i.e. anterior to) the focal plane, they produce positive contrast and conversely, when they are below the focal plane, they produce negative contrast. The curvature of the endothelium is also evident in Fig. 6.

We counted 146 nuclei present in a 273 x 193 μ m region of interest centered in the middle of the field shown in Fig. 6. The density is therefore 2770 cell/mm². This is just below the normal range reported for the 20-29 year-old age group (2942 \pm 116 cells/mm² [28]).

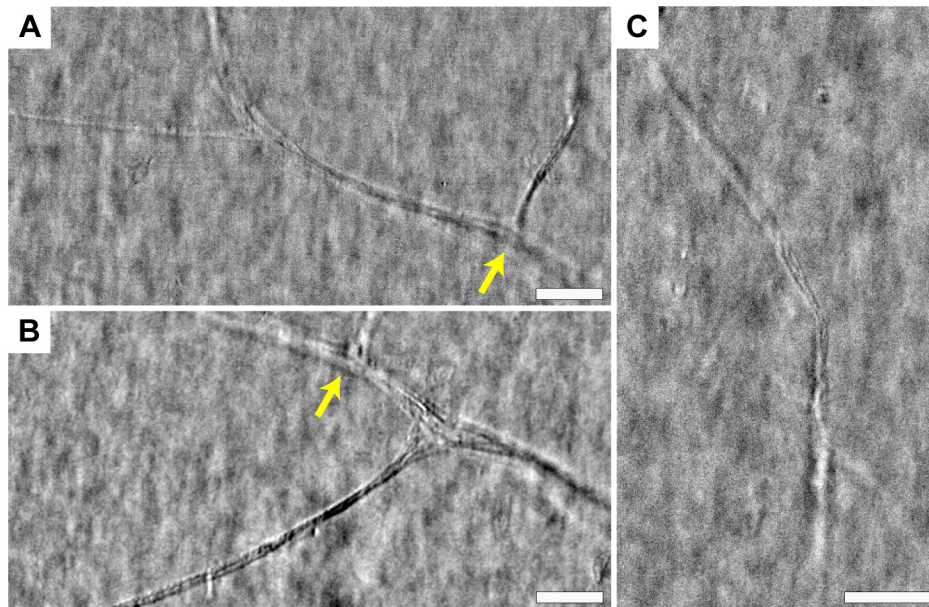


Fig. 5. Stromal nerves in a 28-year-old male. (A) Stromal nerve segment just anterior to view shown in (B). Arrows indicate the same branch point. (C) Stromal nerve in focus near the center and out of focus at the top and bottom. Scale bars: 50 μm .

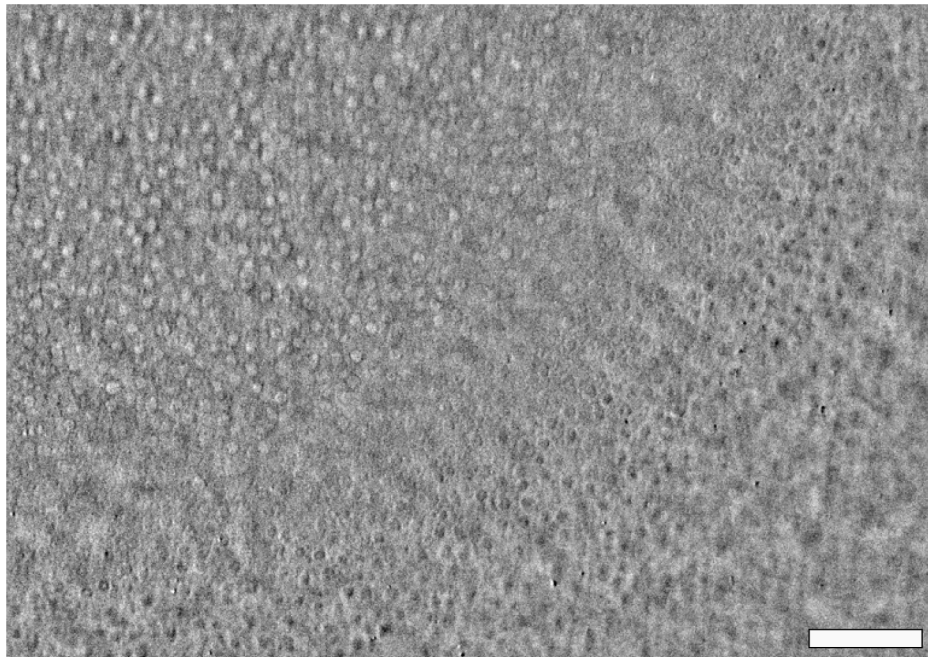


Fig. 6. Endothelium of a 26-year-old female. Bright/dark circles are nuclei anterior or posterior to the focal plane (see [Visualization 2](#) for laterally-stabilized through-focus). Scale bar: 100 μm .

4.5. Crystalline lens

With a 20 mm working distance dry objective lens we can easily adjust the system to image the crystalline lens, which begins about 3.3 mm behind the air-cornea interface. However, ray tracing software indicated that strong spherical aberration, from the air-cornea refractive index mismatch, impedes clear imaging. To reduce sensitivity to aberration, we lowered the effective imaging NA by relaying the objective's back focal plane to an external iris prior to focusing on the camera. Passage through the external iris reduced the imaging NA from 0.4 down to 0.2. Despite the lower resolution, both the lens epithelium and anterior lens fibers were discernible. Example images from a 28-year-old male are shown in Fig. 7.

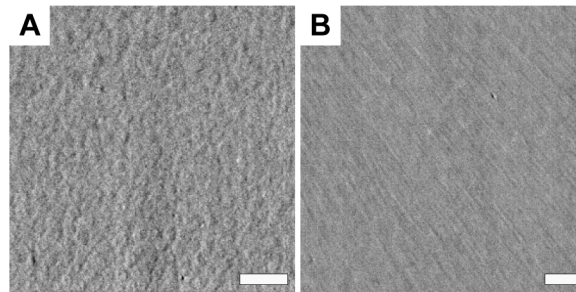


Fig. 7. Crystalline lens (A) epithelium and (B) anterior fibers just below the epithelium. Scale bars 50 μm .

5. Discussion

We have described a new *in vivo* corneal and lenticular imaging method, which we call retroillumination microscopy. The technique is non-contact and produces images with high lateral resolution (1-2 μm), comparable to state-of-the-art IVCN. In contrast with laser-scanning IVCN, retroillumination microscopy is a widefield camera-based technique, meaning all pixels are exposed simultaneously. This enables fast acquisition of large fields of view (3X larger area than current IVCN), which is useful for quantifying subbasal nerves and endothelial cells. An even larger FOV is possible, for instance with a higher resolution camera, however the marginal utility would be limited without compensation for corneal curvature (e.g. Ref. [29]). The large FOV and non-contact operation come partly at the expense of NA, which in a widefield (nonconfocal) imaging configuration, results in reduced axial sectioning strength and contrast. Nevertheless, structures such as corneal epithelial cells, dendritic cells, subbasal and stromal nerves, endothelial cells, lens epithelium and fibers are all recognizable.

The technique is currently limited to the central and paracentral regions of the cornea because the pupil determines the retroilluminated area. More peripheral regions could be accessed if the pupil were chemically dilated, however the limbus would still not be accessible.

Unlike most other *in vivo* eye imaging techniques, retroillumination microscopy is based on transmitted light. This difference has a fundamental impact on obtainable image contrast [8,30]. In order for light reflection, or more precisely, backscattering to occur, the sample must present an abrupt change in refractive index. This could either be an interface (specular reflection) or a clump of scattering structures each smaller than the wavelength of incident light (Rayleigh-like scattering). On the contrary, transmission microscopy is sensitive to forward-scattered light, such as that primarily generated by larger structures, for example spheroid cell bodies or nuclei. A clear example is the different appearance of the corneal endothelium, which in reflection contrast usually appears as a hyper-reflective interface with dark paths delineating cell borders [4]. In transmission contrast, it is the cell nuclei that are most apparent, while cell edges are undetectable

(see Fig. 6). An important exception appears to be keratocyte nuclei, which exhibit better contrast in reflection. This is likely related to their unique flattened shape [6]. As an aside, the adaptive optics ophthalmoscopy community has already recognized the utility of forward scattered light as a method to enhance contrast of blood flow [31], photoreceptor cone inner segments [32], and retinal ganglion cells [33]. There are likely many other corneal features where transmission contrast can contribute complimentary information.

Our method bears resemblance to the well-known slit lamp technique known as retroillumination [15] (n.b. the naming similarity is intentional). Both techniques reflect light off posterior structures in order to back-illuminate the lens and cornea. However, unlike the slit lamp biomicroscope, which features separate, non-overlapping illumination and imaging paths, our system is designed around a single objective lens. With this configuration we are free to use a higher NA in the imaging path without physically obstructing the illumination. Thus our single lens configuration provides higher optical resolution than that obtainable with slit lamps. Similarly, our design enables unimpeded illumination of large fundus areas. We use this freedom to implement asymmetric illumination, a well-established method to enhance phase-gradient contrast [16].

Transmission imaging also avoids superficial sample reflections, such as the prominent corneal anterior surface reflection. Excess background from this reflection can easily dominate intracorneal backscattering. Hence, high optical sectioning strength (e.g. confocal filtering or coherence gating) is normally required to diminish its effect, which in turn increases system complexity. In the absence of this reflection, we are able to form useful *en face* images across a large, 1 mm diagonal FOV with little more than a widefield microscope made of readily available off-the-shelf components.

Retroillumination provides excellent contrast of corneal nerves, particularly the subbasal plexus, which is recognized as a potential noninvasive biomarker for diabetic peripheral neuropathy [34]. Combined with the large FOV and non-contact operation, retroillumination microscopy may be a useful tool for monitoring diabetic neuropathy or other ocular diseases affecting corneal nerves. In addition, retroillumination could play a valuable role in diagnosis of microbial keratitis (i.e. amoebic, fungal, bacterial) [1]. The method may also be more tolerable for children, where cooperation with contact operation is often an issue. In research, the unique ability to visualize corneal endothelial nuclei may be useful for monitoring experimental proliferative therapies to regenerate endothelial cells.

Funding

National Eye Institute (EY029486).

Acknowledgments

TDW would like to thank Neil Lagali for his helpful comments and suggestions.

Disclosures

The authors declare no conflicts of interest.

References

1. P. K. Vaddavalli, P. Garg, S. Sharma, V. S. Sangwan, G. N. Rao, and R. Thomas, "Role of confocal microscopy in the diagnosis of fungal and acanthamoeba keratitis," *Ophthalmology* **118**(1), 29–35 (2011).
2. W. M. Bourne, "Biology of the corneal endothelium in health and disease," *Eye* **17**(8), 912–918 (2003).
3. D. V. Patel and C. N. J. McGhee, "In vivo confocal microscopy of human corneal nerves in health, in ocular and systemic disease, and following corneal surgery: a review," *Br. J. Ophthalmol.* **93**(7), 853–860 (2009).
4. R. A. Laing, M. M. Sandstrom, and H. M. Leibowitz, "In vivo photomicrography of the corneal endothelium," *Arch. Ophthalmol.* **93**(2), 143–145 (1975).
5. R. F. Guthoff, C. Baudouin, and J. Stave, *Atlas of Confocal Laser Scanning In-vivo Microscopy in Ophthalmology* (Springer-Verlag, 2006).

6. S. Bohn, K. Sperlich, S. Allgeier, A. Bartschat, R. Prakasam, K.-M. Reichert, H. Stolz, R. Guthoff, R. Mikut, B. Köhler, and O. Stachs, "Cellular in vivo 3D imaging of the cornea by confocal laser scanning microscopy," *Biomed. Opt. Express* **9**(6), 2511–2525 (2018).
7. D. Huang, E. A. Swanson, C. P. Lin, J. S. Schuman, W. G. Stinson, W. Chang, M. R. Hee, T. Flotte, K. Gregory, C. A. Puliafito, and J. G. Fujimoto, "Optical coherence tomography," *Science* **254**(5035), 1178–1181 (1991).
8. A. F. Fercher, "Optical coherence tomography," *J. Biomed. Opt.* **1**(2), 157–173 (1996).
9. S. Chen, X. Liu, N. Wang, X. Wang, Q. Xiong, E. Bo, X. Yu, S. Chen, and L. Liu, "Visualizing micro-anatomical structures of the posterior cornea with micro-optical coherence tomography," *Sci. Rep.* **7**(1), 10752 (2017).
10. V. Mazlin, P. Xiao, E. Dalimier, K. Grieve, K. Irsch, J.-A. Sahel, M. Fink, and A. C. Boccara, "In vivo high resolution human corneal imaging using full-field optical coherence tomography," *Biomed. Opt. Express* **9**(2), 557–568 (2018).
11. B. Tan, Z. Hosseinaee, L. Han, O. Kralj, L. Sorbara, and K. Bizheva, "250 kHz, 1.5 μ m resolution SD-OCT for in-vivo cellular imaging of the human cornea," *Biomed. Opt. Express* **9**(12), 6569–6583 (2018).
12. X. Yao, K. Devarajan, R. M. Werkmeister, V. A. dos Santos, M. Ang, A. Kuo, D. W. K. Wong, J. Chua, B. Tan, V. A. Barathi, and L. Schmetterer, "In vivo corneal endothelium imaging using ultrahigh resolution OCT," *Biomed. Opt. Express* **10**(11), 5675–5686 (2019).
13. C. Canavesi, A. Cogliati, A. Mietus, Y. Qi, J. Schallek, J. P. Rolland, and H. B. Hindman, "In vivo imaging of corneal nerves and cellular structures in mice with gabor-domain optical coherence microscopy," *Biomed. Opt. Express* **11**(2), 711–724 (2020).
14. E. Auksoy, D. Borycki, P. Stremplewski, K. Liżewski, S. Tomczewski, P. Niedźwiedziuk, B. L. Sikorski, and M. Wojtkowski, "In vivo imaging of the human cornea with high-speed and high-resolution fourier-domain full-field optical coherence tomography," *Biomed. Opt. Express* **11**(5), 2849–2865 (2020).
15. N. Brown, "Visibility of transparent objects in the eye by retroillumination," *Br. J. Ophthalmol.* **55**(8), 517–524 (1971).
16. B. Kachar, "Asymmetric illumination contrast: A method of image formation for video light microscopy," *Science* **227**(4688), 766–768 (1985).
17. S. B. Mehta and C. J. R. Sheppard, "Quantitative phase-gradient imaging at high resolution with asymmetric illumination-based differential phase contrast," *Opt. Lett.* **34**(13), 1924–1926 (2009).
18. T. N. Ford, K. K. Chu, and J. Mertz, "Phase-gradient microscopy in thick tissue with oblique back-illumination," *Nat. Methods* **9**(12), 1195–1197 (2012).
19. T. D. Weber and J. Mertz, "Non-mydratic chorioretinal imaging in a transmission geometry and application to retinal oximetry," *Biomed. Opt. Express* **9**(8), 3867–3882 (2018).
20. N. Streibl, "Three-dimensional imaging by a microscope," *J. Opt. Soc. Am. A* **2**(2), 121–127 (1985).
21. S. B. Reddy and B. N. Chatterji, "An FFT-based technique for translation, rotation, and scale-invariant image registration," *IEEE Trans. on Image Process.* **5**(8), 1266–1271 (1996).
22. E. Meijering, M. Jacob, J.-C. Sarria, P. Steiner, H. Hirling, and M. Unser, "Design and validation of a tool for neurite tracing and analysis in fluorescence microscopy images," *Cytometry* **58A**(2), 167–176 (2004).
23. C. A. Schneider, W. S. Rasband, and K. W. Eliceiri, "NIH Image to ImageJ: 25 years of image analysis," *Nat. Methods* **9**(7), 671–675 (2012).
24. P. Thevenaz, U. E. Ruttimann, and M. Unser, "A pyramid approach to subpixel registration based on intensity," *IEEE Trans. on Image Process.* **7**(1), 27–41 (1998).
25. M. Parissi, G. Karanis, S. Randjelovic, J. Germundsson, E. Poletti, A. Ruggeri, T. P. Utheim, and N. Lagali, "Standardized baseline human corneal subbasal nerve density for clinical investigations with laser-scanning in vivo confocal microscopy," *Invest. Ophthalmol. Visual Sci.* **54**(10), 7091–7102 (2013).
26. L. Mastropasqua, M. Nubile, M. Lanzini, P. Carpineto, M. Ciancaglini, T. Pannellini, M. Di Nicola, and H. S. Dua, "Epithelial dendritic cell distribution in normal and inflamed human cornea: in vivo confocal microscopy study," *Am. J. Ophthalmol.* **142**(5), 736–744 (2006).
27. C. F. Marfurt, J. Cox, S. Deek, and L. Dvorscak, "Anatomy of the human corneal innervation," *Exp. Eye Res.* **90**(4), 478–492 (2010).
28. R. W. Yee, M. Matsuda, R. O. Schultz, and H. F. Edelhauser, "Changes in the normal corneal endothelial cellular pattern as a function of age," *Curr. Eye Res.* **4**(6), 671–678 (1985).
29. V. Mazlin, K. Irsch, M. Paques, M. Fink, and A. C. Boccara, "Curved-field optical coherence tomography: large-field imaging of human corneal cells and nerves," <https://arxiv.org/abs/2004.01016>.
30. A. Sentenac and J. Mertz, "Unified description of three-dimensional optical diffraction microscopy: from transmission microscopy to optical coherence tomography: tutorial," *J. Opt. Soc. Am. A* **35**(5), 748–754 (2018).
31. T. Y. P. Chui, D. A. VanNasdale, and S. A. Burns, "The use of forward scatter to improve retinal vascular imaging with an adaptive optics scanning laser ophthalmoscope," *Biomed. Opt. Express* **3**(10), 2537–2549 (2012).
32. D. Scoles, Y. N. Sulai, C. S. Langlo, G. A. Fishman, C. A. Curcio, J. Carroll, and A. Dubra, "In vivo imaging of human cone photoreceptor inner segments," *Invest. Ophthalmol. Visual Sci.* **55**(7), 4244–4251 (2014).
33. E. A. Rossi, C. E. Granger, R. Sharma, Q. Yang, K. Saito, C. Schwarz, S. Walters, K. Nozato, J. Zhang, T. Kawakami, W. Fischer, L. R. Latchney, J. J. Hunter, M. M. Chung, and D. R. Williams, "Imaging individual neurons in the retinal ganglion cell layer of the living eye," *Proc. Natl. Acad. Sci.* **114**(3), 586–591 (2017).

34. S. Misra, J. Craig, D. Patel, C. McGhee, M. Pradhan, K. Ellyett, D. Kilfoyle, and G. Braatvedt, "In vivo confocal microscopy of corneal nerves: An ocular biomarker for peripheral and cardiac autonomic neuropathy in type 1 diabetes mellitus," *Invest. Ophthalmol. Visual Sci.* **56**(9), 5060–5065 (2015).